



General assembly rules for metamaterials with scalable twist effects

Weiyun Xu^{a, #}, Liwei Wang^{a, #}, Zhao Liu^{b,*}, Ping Zhu^{a,*}

^a The State Key Laboratory of Mechanical System and Vibration, National Engineering Research Center of Automotive Power and Intelligent Control, School of Mechanical Engineering, Shanghai Jiao Tong University, Shanghai, China

^b School of Design, Shanghai Jiao Tong University, Shanghai, China



ARTICLE INFO

Keywords:
Metamaterials
Chiral
Twist effects
Screw theory
Scalable

ABSTRACT

Metamaterials with twist effects can exhibit remarkable rotational deformation under tension or compression, a behavior that is uncommonly observed in conventional materials. Despite its promise in achieving complex engineering functionalities, the twist effect is unscalable and will quickly diminish as the number of unit cells increases, which is the major restriction for practical applications. In this study, we use screw theory to rigorously analyze the relationship between microscale geometries and twist effects, unraveling the mechanism underlying the loss of scalability. We further propose a general assembly rule for metamaterial crystals to achieve scalable effects. A simplified analytical model is developed to characterize the scalability of the twist. Through simulation, analytical models, and physical experiments, we demonstrate the flexibility and superiority of the proposed assembly rules in enabling scalable twist effects for various unit-cell designs, different strain levels, and even twists around multiple axes. This constitutes an important step towards scaling up the twist effects for real applications.

1. Introduction

Metamaterials are artificial materials that derive properties mainly from the geometry of microstructures rather than constituent materials [1–4]. Their properties can go beyond that of their constituents and even enable unprecedented behaviors that were previously not found in nature [5–7]. For mechanical metamaterials, while most research focuses on rendering extreme and counterintuitive mechanical properties, such as negative Poisson's ratio [8–10], multi-stable states [11,12], and vanishing shear modulus [13,14], these metamaterials are still considered as Cauchy continuum with zero force-torque couplings. Recently, metamaterials with additional twist degrees of freedom (DOF) have been proposed to realize this force-torque coupling [15,16], ushering the research into the regime of the micropolar Eringen continuum [17,18]. As an essential deformation form of materials and structures, the phenomenon of twist plays an important role in nature and engineering systems, e.g., humidity-driven twist in spider silk [19,20], twist-under-tension in DNA [21], as well as inversion and perversion effect in cylindrical tubes [22]. By assembling rationally designed unit cells, metamaterial crystals can be obtained to achieve twisting upon pushing or pulling (Fig. 1, a and b). This twist effect provides higher

flexibility in tuning the mechanical responses and is potentially useful for complicated functionalities, such as mechanical cloaking [23,24], actuators in soft robotics [25,26], and conversion of transverse mode in acoustic devices [27,28].

Due to this promise, considerable progress has been made in designing various metamaterials with twist effects [29–35]. For example, metamaterial crystals composed of cubic-symmetric unit cells [36–40] or uniaxial chiral auxetics [41–45], tubular metastructures utilizing planar shearing motifs [46–50], alternative combinations of chiral and achiral lattices [51–55], and other chiral unit cells with noncubic crystal symmetry (octahedra, dodecahedron, or icosahedron) [16,56]. And the rationality underlying some of these mainstream intuitive designs was verified by a topological method based on couple-stress homogenization [57]. Furthermore, the inherent mechanism of the microstructure-twist relationship has been investigated. Li et al. [58] have clarified the compression-to-shear and compression-to-torsion effects of two-dimensional (2D) and three-dimensional (3D) microstructures respectively in a mechanical way. The twist properties in one or more principal directions vary for different microstructures and can be modulated by tuning the geometrical parameters of the rod components. Generally, a 3D metamaterial

* Corresponding author.

E-mail addresses: hotlz@sjtu.edu.cn (Z. Liu), pzhu@sjtu.edu.cn (P. Zhu).

The two authors contributed equally to this work.

crystal with twist effect can be viewed as an assembly of a set of 2D chiral components [36,57,59,60]. And cubical unit cells are practically more suitable for assembling metamaterials with massive unit cells considering boundary connectivity [16]. Typical cubic unit cells of metamaterial with twist effects include Z-shaped [58,61], O-shaped [16, 62], and #-shaped [58,63] topologies, which can be decomposed into Z-shaped, O-shaped, and #-shaped 2D motifs respectively.

However, the twist effect in existing designs [15,16,43,64] is unscalable, which means that the twist angle will diminish for a large number of assembled unit cells. Specifically, suppose an $L_x \times L_y \times L_z$ metamaterial crystal is composed of $N_x \times N_y \times N_z$ cubic unit cells, each of size $a_x \times a_y \times a_z$, the crystal renders a twist angle θ upon imposing a compression strain ϵ on the top. For ease of illustration, we define a scale factor N and assume $N_x \propto N_y \propto N_z \propto N$, i.e., the number of unit cells may vary along different directions but will be in the same order and proportionate to the scale factor N . As shown in Fig. 1(c), the twist angle per axial strain θ/ϵ decreases rapidly and may eventually fall to zero as N increases [15], asymptotically following a decreasing curve $\propto 1/N$. In existing designs [15,16,43,64], a significant drop in the twist angle can be observed even for a very small scale factor, i.e., $N \leq 5$. For example, the twist angle per strain of a recently proposed crystal [16] drops by half when N goes from 1 to 5 under a 1% strain. Due to the loss of scalability, the generalized Eringen continuum degenerates to a conventional Cauchy continuum with little or no twist effect [65]. As a result, the applications of metamaterials with the twist effect are restricted to small samples and simple components.

Intuitively, the loss of scalability is due to the incompatible twists of neighboring unit cells on the shared boundaries. It leads to the geometrical frustration between unit cells inside the crystals, i.e., the preferred deformation of neighboring unit cells cannot be simultaneously satisfied due to interactions. In contrast, unit cells on the crystal surface have fewer interactive bonds and thus contribute most to the overall twist. As N increases, the inner unit cells with little twist effect outnumber those on the surface and dominate the overall deformation behaviors. The ratio between the surface and the inner volume of the crystal asymptotically decreases as $1/N$, and so is the twist angle per axial strain θ/ϵ .

In the last few years, attempts have been made to relieve the geometrical frustration inside the crystals by weakening the bonding between neighboring unit cells, either by connecting them with compliant structures [55] or carefully designed connectors [65]. With the weakened bonds, the twist angle can remain at a stable level and even slightly increases when N goes to 5~10. While this improvement

represents a major step forward in achieving scalability, the twist angle still asymptotically decreases as N goes beyond a certain threshold (typically around 10) [65]. Further improvement is possible for these crystals but at the cost of significantly reducing stiffness and integrity. Moreover, these modifications are heuristically devised for a specific type of unit cell and only demonstrated for single-axial twists. It is not straightforward how to extend them to general unit-cell designs and enable scalable multi-axial twists.

The aim of this study is thus to develop a general design rule for elastic metamaterials to achieve scalable twist effects, accommodating different unit-cell designs and multi-axial twists. In our view, the twist of the crystal implies a rotational invariance of the overall deformation around the center axis, which contradicts the translational invariance of the geometry inherited from the periodic unit-cell assembly. This intrinsic inconsistency determines that scalable tension-twist behaviors cannot be realized with periodic assembly. Reducing the strength of bonding without altering the assembly can only partially relieve the incompatibility. Therefore, instead of modifying the unit-cell designs, we adopt a completely different strategy by designing the assembly pattern to ensure compatible twists between unit cells. We note that most of the current research on the unscalable twist effect relies on intuitive analysis. While it can provide heuristics for the unit-cell design in a periodic crystal, it falls short to guide the design of the assembly pattern, which involves an immense combinatorial design space and the complex interaction between unit cells.

To address this issue, we propose to use the screw theory [66] as an effective tool to analyze the collective behaviors of assembled unit cells in a rigorous way. Based on the insights obtained from the screw theory, a general assembly rule is proposed to replace the periodic assembly for scalable twist effects. In Section 2, a simplified analytical model was developed to characterize the relation between N and twist angle per axial strain θ/ϵ . In Section 3, the assembly rule was applied to various cubic unit-cell designs and crystals with multiple strain levels, different ranges of geometrical parameters, and even multi-axis twists. The analytical model, finite element analysis (FEA), and experiments on 3D-printed samples matched well to validate the scalable twist effects. In all the cases, the twist angles quickly converged to a constant level and remained stable as the N increases (even up to $N = 20$), demonstrating superior scalability that was previously unachievable. Finally, we draw the conclusions in Section 4.

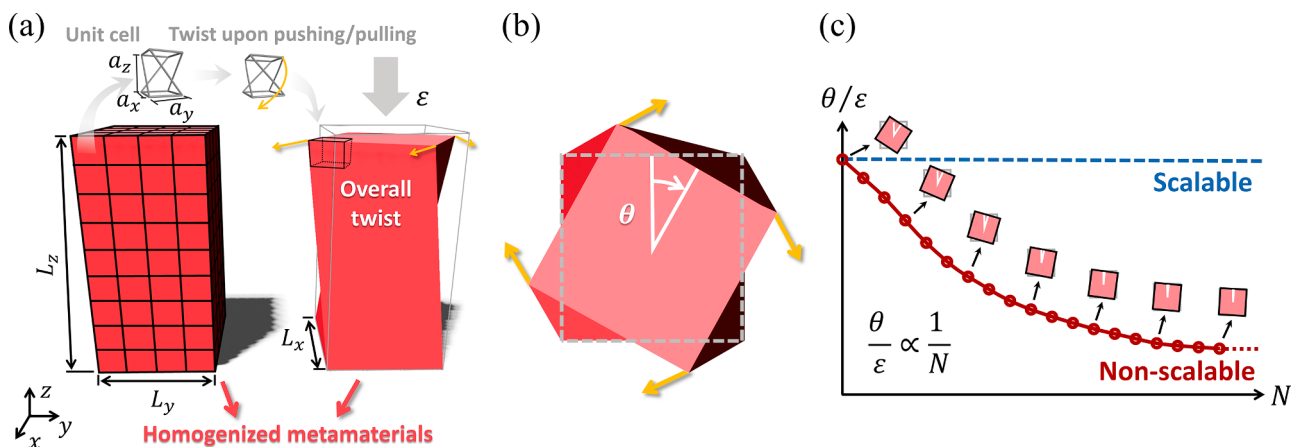


Fig. 1. Illustration of the twist effect and the loss of scalability. (a) Metamaterial crystal (left) composed of rationally-designed unit cells with the twist effect. The unit-cell deformation leads to an overall twist (right) upon the normal strain. For the sake of simplicity in our illustrations, we present the crystals as homogenized solids, omitting the specific details of their unit cells. (b) Vertical view of the twisted crystal with the twist angle θ marked. The dashed box represents the undeformed contour while the yellow arrows show the twisting direction. (c) The schematic diagram for the relation between θ/ϵ and N . Dashed and solid lines are for scalable and unscalable cases, respectively. The floating inset for each scattering point corresponds to the vertical view as in (b).

2. Material and methods

In this section, we analyzed the twist effects underlying the metamaterial crystals based on screw theory, characterizing the criteria that guarantee compatible twisting among unit cells. Thereafter, we introduced the finite element analysis (FEA) of metamaterial crystals and the experimental methods to validate the criteria.

2.1. Screw-theory-based analysis on twist effects

To facilitate the analysis of the deformation, we consider unit-cell designs with twist effects as flexible compliant mechanisms [67,68], in which multiple components combine to realize a single twist DOF. An instant pseudo-rigid-body model (PRBM) [11,60] can then be created for the mechanism to simplify the description of the overall behavior (Fig. 2a and b). It models flexible components as rigid segments connected by revolute joints, ignoring the local deformation within each component but permitting rotation around artificial revolute joints. We then apply screw theory to the simplified PRBM to analyze its motional DOF, which can elucidate the mechanism underlying the issue of unscalability and provide insights to mitigate it. Before diving into the detailed analysis of PRBM, it is crucial to clarify that this model is exclusively employed for assessing the instantaneous degree of freedom from a kinematic perspective. We will also utilize the PRBM to elucidate the simulation and experimental results, deriving theoretical twisting angles within a simplified framework. Remarkably, considering the

small deformations in this study, we have observed that the instantaneous pseudo-rigid-body model provides commendable predictions of the twist angle. We will unfold this in subsequent sections that include simulations and experiments. Herein, we use the simple Z-shaped unit cell [58] for demonstration, while the same analysis can be applied to other unit-cell types and will be illustrated in later parts.

The screw theory [66] is based on the observation that, any instantaneous motion or external constraint of a rigid body (Fig. S1) can be viewed as a combination of a translational component along and a rotational component around an instantaneous screw axis (ISA). Screw representation is introduced to simultaneously describe these two types of components and the ISA, for both motions and constraints (see Supplementary File text S1 for details). It enables the use of rigorous algebraic theory to analyze the kinematic behaviors of a system assembled by multiple parts. For a unit cell with twist effects, the twist DOF of the instant PRBM can be described by a motion screw $\xi = \omega[\tilde{e}, h\tilde{e}]^T$ with an angular velocity ω , a finite pitch h , and the center line \tilde{e} as its ISA, as shown in Fig. 2(e) to (h). Similarly, the constraints within the unit cell can also be described by a set of constraint screws $\{\zeta_i\}$. To achieve the twist DOF ξ , ISA e_i of each constraint ζ_i should belong to the same branch of straight lines on a hyperbolic surface of one sheet (HS-1) centering around \tilde{e} (Fig. 2, e and f; see detailed discussion in text S1). To put it more rigorously, the constraint screw should have the form as $\zeta_i = [\mathbf{e}_i, \mathbf{r}_i \times \mathbf{e}_i]^T$, where \mathbf{r}_i is a vector connecting the unit-cell center \tilde{o} and a point on ISA. By requiring $\tilde{e} \cdot \mathbf{e}_i > 0$, the sign of $\tilde{e} \cdot \mathbf{r}_i \times \mathbf{e}_i$ can be used to differentiate the two branches of straight lines on HS-1, which should be the

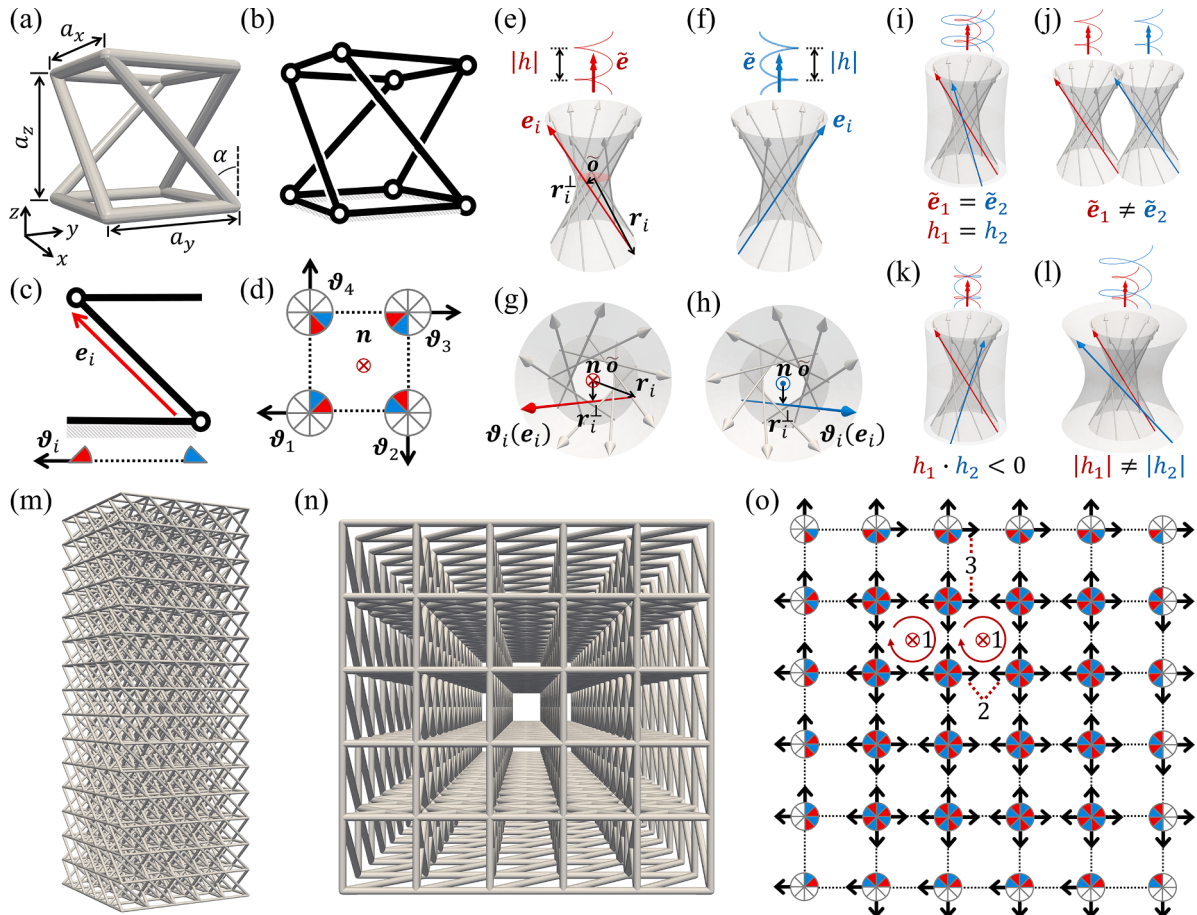


Fig. 2. Screw-theory-based analysis of the metamaterial crystal with twist effects. (a) Z-shaped unit cell and (b) its instant PRBM. (c) 2D description of a basic component and its constraint screw, (d) 2D description of the unit-cell structure and its screw system. (e) and (f) show screw systems with the constraint screws corresponding to the two branches on straight lines on HS-1, respectively, their top-view plots are shown in (g) and (h). (i) shows the compatible motions between unit cells, and (j) to (l) show three forms of incompatible screw systems. (m) Periodic crystal assembled by the Z-shaped unit cell. (n) Top-view and (o) 2D description of the crystal in (m). The numerical labels '1', '2', and '3' mark different incompatible cases.

same for all ξ_i . The pitch of ξ can be obtained as

$$h = \frac{-\tilde{\mathbf{e}} \cdot (\mathbf{r}_i \times \mathbf{e}_i)}{\tilde{\mathbf{e}} \cdot \mathbf{e}_i} = \frac{\mathbf{r}_i^\perp \cdot (\tilde{\mathbf{e}} \times \mathbf{e}_i)}{\tilde{\mathbf{e}} \cdot \mathbf{e}_i} \quad (1)$$

where $\mathbf{r}_i^\perp = r\mathbf{e}_r$, i is the vector starting from \tilde{o} and perpendicularly connecting to the ISA of ξ_i , with a length of r .

To facilitate later analysis, we develop a 2D description for the screw system of a unit cell. Specifically, we first identify the basic component that provides a single constraint screw ξ_i , e.g., the Z-shaped component in Fig. 2(c). We then project constraint ISA \mathbf{e}_i to the normal plane of twist ISA $\tilde{\mathbf{e}}$, obtaining a vector ϑ_i to represent ξ_i from the vertical view (Fig. 2g). The abstract 2D notation in Fig. 2(d) can then be used to simultaneously describe screws and geometries in 2D. The red and blue patches represent the top and bottom nodes of the basic component while ϑ_i points from blue to red. When ISA of $\{\xi_i\}$ are straight lines on HS-1 of the same branch, $\{\vartheta_i\}$ will be aligned on a directed circle centered at \tilde{o} , with the path direction denoted by a normal vector \mathbf{n} based on the right-hand rule. The sign of $\tilde{\mathbf{e}} \cdot \mathbf{n}$ in the 2D description is equivalent to $\tilde{\mathbf{e}} \cdot \mathbf{r}_i \times \mathbf{e}_i$ in Eq. (1). Therefore, the positive (negative) sign of $\tilde{\mathbf{e}} \cdot \mathbf{n}$ corresponds to the right (left) handedness of the unit-cell structures. Suppose the unit cell twists around the z axis, i.e., $\tilde{\mathbf{e}} = \mathbf{e}_z$, the twist angle per uniaxial strain (for this instant PRBM) is given as

$$\theta = \frac{\theta}{\theta h/a_z} = \frac{a_z}{h} = \frac{a_z}{r} \frac{\mathbf{e}_z \cdot \mathbf{e}_i}{\mathbf{e}_{r,i} \cdot (\mathbf{e}_z \times \mathbf{e}_i)}. \quad (2)$$

Since $\mathbf{e}_z \cdot \mathbf{e}_i > 0$, it can be concluded from Eq. (1) and Eq. (2) that a right (left)-handed unit cell corresponds to a negative (positive) pitch h of the twist screw, which induces a rotation along the positive (negative) z -axis upon compression. In particular, for a Z-shaped unit cell with the diagonal bars tilted at an angle $\alpha \in (-\pi/2, \pi/2)$ to the z -axis (Fig. 2a), we can obtain $h = \frac{a_z}{2} \tan(\alpha)$ and $\frac{\theta}{\epsilon} = 2 \frac{a_z}{a_x} \cot(\alpha) = 2 \cot^2(\alpha) = 2 \left(\frac{a_z}{a_x} \right)^2$. When $\alpha > 0$, the unit cell has right-handedness ($h > 0$) and a negative twisting angle ($\theta < 0$) upon compression ($\epsilon < 0$). It can also be noted that the twisting angle per uniaxial strain only depends on the aspect ratio $\frac{a_z}{a_x}$ or the angle α of the unit cell. The above analysis is based on the instant PRBM without considering the elastic deformation within the components. Therefore, the rotational angle in Eq. (2) might deviate from the value obtained under the elastic settings. Nevertheless, this analysis provides a concise and quantitative tool to elucidate the relation between the unit-cell geometry and its twist.

To extend the analysis to a crystal, we can follow a similar procedure to obtain the PRBM of the whole crystal and identify the constraint screws. To realize an overall twist DOF with the crystal, these constraint screws should also reside on one or multiple HS-1. Ideally, constraint screws on different HS-1 should correspond to the same motion screw as shown in Fig. 2(i), i.e., with the same ISA $\tilde{\mathbf{e}}$ and pitch value h_b to ensure compatible motions between unit cells. However, existing designs do not meet this requirement. In these crystals, the constraint screws induce multiple incompatible motion screws that have different ISA (Fig. 2j), pitches with contrary signs (Fig. 2k), or pitches with different magnitudes (Fig. 2l). For example, the screw system for the periodically assembled Z-shaped unit cells (Fig. 2, m and n) contains all three forms of incompatibilities (Fig. 2o):

- i) ISA of constraints screws in each unit cell belongs to an HS-1 around its own unit-cell center, but not the center of the crystal (see the two HS-1 marked by '1' in Fig. 2o).
- ii) Constraints screws belong to different branches of straight lines (see the two screws labeled by '2' in Fig. 2o).
- iii) Constraint screws belong to HS-1 around the center of the crystal but with various radius values, corresponding to different pitches of motion screws (see the two screws labeled by '3' in Fig. 2o).

Due to these incompatible screws, the crystals undergo elastic

frustration in the twist motion that will reduce the twisting angle. The loss of scalability happens when incompatible screws dominate as N increases. This screw-based analysis explains the non-scalability rigorously and quantitatively, unraveling multiple forms of incompatibility that are difficult to identify in previous intuitive analyses. In the remaining parts, we will demonstrate how to use these insights to achieve scalable twist effects.

2.2. Finite element analysis of metamaterial crystals

In this research, the finite element analysis (FEA) is carried out by ABAQUS to simulate the deformation of mechanical metamaterials with twist effects under a given compression. The size of the crystal is set to be $L_z = 3L_x = 3L_y = 225\text{mm}$, which is the same as that in the physical experiment. The constituent material adopted in the simulation is consistent with that of fabricated samples, which is nylon PA12 with Young's modulus of 1500MPa and Poisson's ratio of 0.3. We adopt linear elasticity for the constitutive behaviors of the material while incorporating geometrical nonlinearity in FEA. To avoid the unaffordable computational cost, we use a fine mesh of B31 beam elements instead of solid elements for the finite element models. In this way, we can perform the simulation for all the metamaterial crystals in the main text including $N = 20$ which is meshed by more than 660 thousand elements with characteristic length at 0.3mm. To guarantee the uniaxial compressive boundary condition, an axial displacement $\Delta h = \epsilon L_z$ is imposed on the top of the crystal with the bottom fixed. The nodes on the top surface are coupled by a reference point at the top center. Thus, the overall twist angle θ can be easily calculated from the displacement of any node on the top with respect to the reference point. The twist angle per uniaxial strain is then calculated by $\theta/\epsilon = \theta_0 L_z / \Delta h$.

As N increases, the size of unit cells and the section of their components will be scaled down accordingly, i.e., by $1/N$. For all the crystals, we assume a circular section for the component, and so is its beam element. However, we assume a rectangular section when comparing different unit-cell designs in Fig. 5(j). This is because the O-shaped unit cell proposed by Frenzel et al. [16] has a rectangular section of its components. We keep this setting for all the unit cells to ensure a fair comparison.

2.3. Fabrication and physical test of metamaterial crystals

In order to validate the proposed rules, we fabricated all the samples of metamaterial crystals as shown in Fig. 3(a) through a commercial 3D selective laser sintering (SLS) printer ProX SLS 6100, using nylon PA12 as the constituent. Nylon PA12 has Young's modulus of 1500 MPa (ISO527-1/-2 and ISO 178) and Poisson's ratio of 0.3. The size of the crystal is set to be $L_z = 3L_x = 3L_y = 225\text{mm}$. A 10-mm-thick solid plate was also printed at both ends of the sample to be clamped by the customized fixture in the experiment. The corresponding boundary conditions are equivalent to that of the FEA model.

We subjected the 3D printed samples to in-situ quasi-static uniaxial compression using a universal testing machine, Bairoe WDW-5, mounted with a 10kN-range load cell. As shown in Fig. 3, the test system was composed of a loading module and a measuring module. In the loading module, the top of the samples was fixed by a customized steel fixture with bolt-assembled clamping heads, and axial forces were imposed by the universal test machine on the top. The axial twist DOF of the samples was released by a thrust bearing in the lower clamping head, which ensures the accurate measurement of test data afterward. In the measuring module, a current-type angle sensor with an accuracy of $0.045^\circ/90.000^\circ$ was used to measure the twist angle differences between the two ends of the sample, and the axial displacement was recorded by an extensometer. An RS485 acquisition card was used to record the twist angle and displacement data. While the structures were being loaded, the angle sensor recorded the twist angle in-situ. In order to reduce experimental errors, the test for each sample was conducted

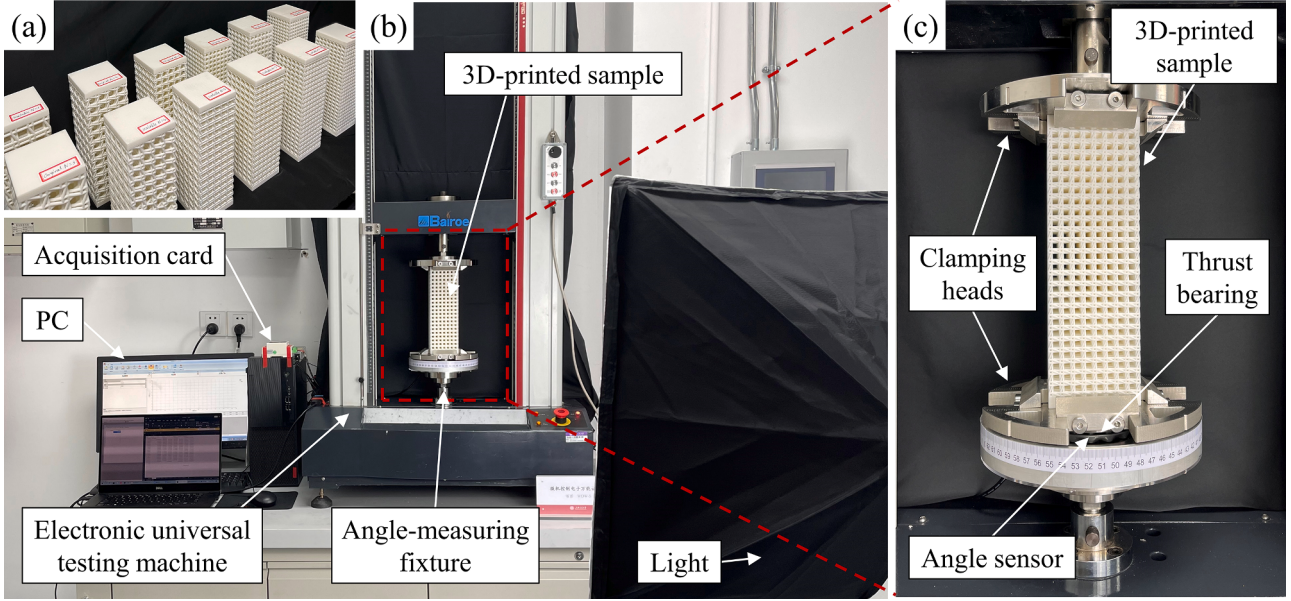


Fig. 3. The settings for the experimental verification. (a) 3D-printed nylon samples of metamaterial crystals. (b) The experimental platform is composed of an electronic universal testing machine and a PC. The light was for photographic use only. (c) The customized angle-measuring fixture is integrated with a thrust bearing and an angle sensor at the bottom.

three times to get an average value.

3. Results and discussion

In this section, we first demonstrated the scalable twist effects around a single axis by applying the proposed general assembly rules to Z-shaped metamaterials. Next, we applied the proposed rule to more

complex metamaterials to study and discussed the scalability of the twist effects. Finally, we further extended the assembly rules to multiple axes to allow the scalable twist under compression from multiple directions.

3.1. Scalable twist effects around a single axis

As illustrated earlier, there are three forms of incompatibility in the

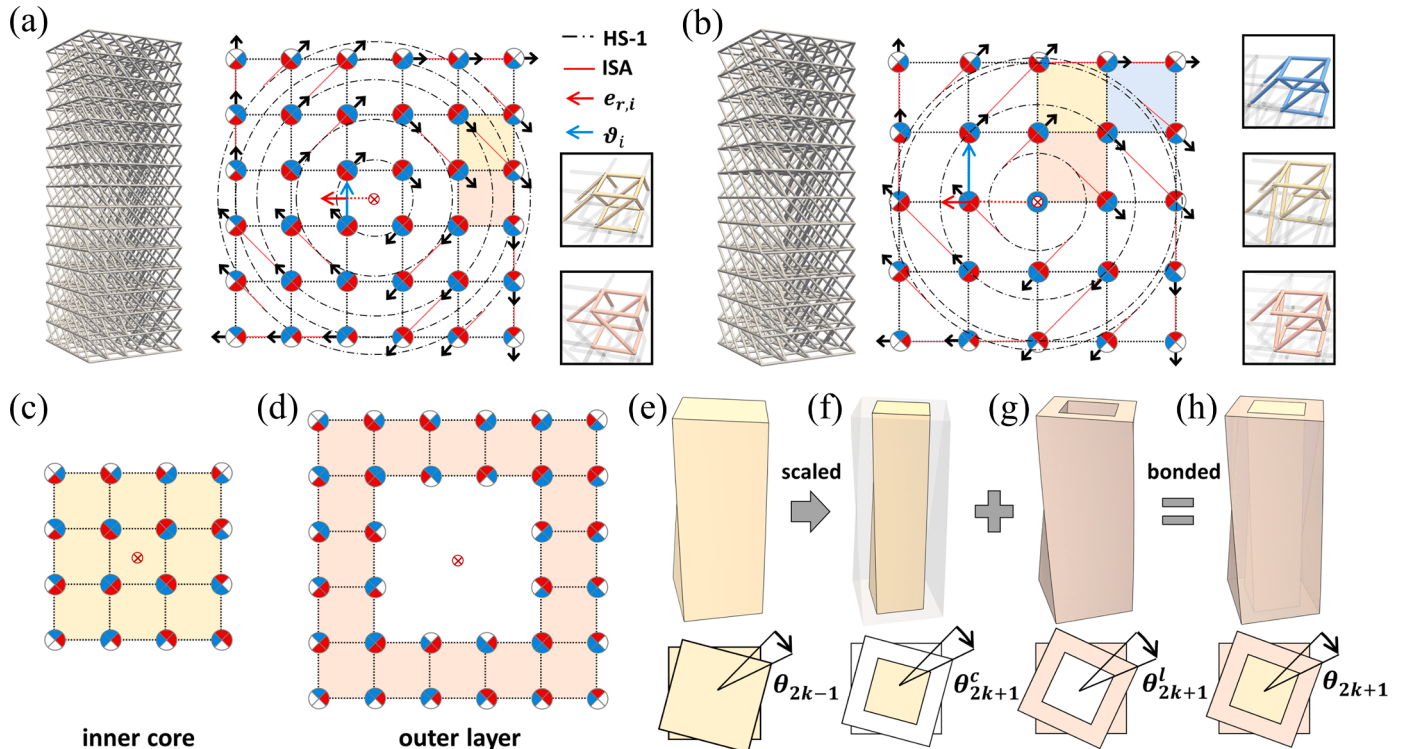


Fig. 4. Proposed assembly rules and the analytical model. (a) An odd-crystal (left) and the corresponding assembly rule (right), with insets showing the detailed geometries of shaded regions with the same colors. In each lattice point, the black arrow shows the projected ISA of its composite constraint screw. (b) Even-crystal and its assembly rule. (c) Inner core and (d) the outer layer of a $2k+1$ crystal. (e) Twisted homogenized solids of $2k-1$ crystal, (f) the stand-alone inner core, (g) the stand-alone outer layer, and (h) the whole $2k+1$ crystal.

screw system of a crystal that will cause frustration. Among them, the frustration induced by the incompatibility in pitch magnitudes will only average unit-cell twists with different pitches. As long as all pitches remain at a finite level, this incompatibility alone does not lead to the loss of scalability. In contrast, frustration induced by the other two forms of incompatibilities will cancel off the twists enabled by different sets of constraints screws. Therefore, these two types of incompatibilities are the main causes of unscalability and should be avoided. To achieve this, for any subsets of the constraints screws residing on HS-1, their reciprocal twist screws should have the same ISA and sign of pitches. With the 2D description, this requirement can be concisely stated as $v_{r,j}^n \cdot (ez \times v_j^n) \equiv A$, where v_j^n is the projected ISA of the composite constraint at node j , $v_{r,j}^n$ is the corresponding normalized radical vector, i.e., r^\perp in Eq. (1), and $A \in \{-1, 1\}$ is the sign of the pitch for the twist screw. While many assembly rules can meet these requirements (see Supplementary File text S2 for detailed discussion), we chose to use one that is simpler in form, more uniform in the stiffness within the crystal, and easier to generalize for other unit-cell designs, as shown in Fig. 4(a) and (b).

Herein, for ease of illustration, we continue to use the Z-shaped unit cell with left-handedness (Fig. 2a) as the demonstrative case. In the assembly rule, we keep all the basic components (Z-shaped bars) in the original periodic assembly but realign their directions to make the projected ISA θ_i satisfy $e_{r,i} \cdot \theta_i \geq 0$. The equal sign is only for components that are in line with the crystal center. This equal sign is a special case for odd crystals, i.e., crystals with odd N as shown in Fig. 4(b), whose crystal center locates on the lattice points instead of the center of the unit-cell face.

To gain more insights into the proposed assembly, we develop an analytical model to describe the relation between N and θ/ϵ . As illustrated earlier, crystals with odd scale factors have the rotation center located on a lattice point while the center of their even counterparts resides on a unit-cell face. Therefore, these two cases may have different twisting behaviors and require different theoretical models. We first focus on crystals with odd scale factors, i.e., $N = 2k - 1$, $k \in N^+$, denoted as $2k - 1$ crystal. We view it as a homogeneous continuum with a twisting angle θ_{2k-1} upon a given strain ϵ (Fig. 4e). For a $2k + 1$ crystal, it can be decomposed into an inner core and an outer layer, as shown in Fig. 4(c) and (d). The core alone (Fig. 4f) will achieve a twisting angle θ_{2k+1}^c upon the strain ϵ while the outer layer alone (Fig. 4g) leads to θ_{2k+1}^l . Meanwhile, the core can also be obtained by first scaling the $2k - 1$ crystal and then increasing the number of unit cells in the z-axis to retain the height L_z (Fig. 4, e and f). Since the twist angle per strain is dimensionless, it remains the same after the scaling, so that $\theta_{2k+1}^c = \theta_{2k-1}$ upon the same strain ϵ . By wrapping the outer layer around the inner core to obtain the $2k + 1$ crystal (Fig. 4h), the twisting angles of the core and layer even off to reach θ_{2k+1} as a new equilibrium, whose value will lie in between θ_{2k+1}^c and θ_{2k+1}^l . By using the linear elastic beam model to describe the twisting of the core and outer layers in the new equilibrium, we can relate θ_{2k+1} and θ_{2k-1} by a recursive expression (see Supplementary File text S3 for detailed derivation)

$$\theta_{2k+1} = \frac{\gamma(2k-1)\theta_{2k-1} + \theta^l}{\gamma(2k-1) + 1}, \quad (3)$$

where $\gamma > 0$ and θ^l are constants to be determined. γ depends on the assembly of both the outer layer and inner core, while θ^l only depends on the assembly of the outer layer. It can be proved that θ_{2k+1} will converge to the constant θ^l as k goes to infinity (see text S3 for detailed proof). The same analysis and conclusions are also applicable to crystals with even scale factors to obtain

$$\theta_{2k+2} = \frac{\tilde{\gamma}(2k)\theta_{2k} + \tilde{\theta}^l}{\tilde{\gamma}(2k) + 1}. \quad (4)$$

Since the assembly of the outer layer does not relate to the parity of

the scale factor, we can assume $\theta^l = \tilde{\theta}^l$. By comparing Eq. (3) and Eq. (4), it can be expected that even-crystals might have their twisting angles different from their odd counterparts for small N . This is because the initial twist angles (θ_1 and θ_2) and the two constants (γ and $\tilde{\gamma}$) are different, which relates to the difference in the assemblies of inner cores. However, the twisting angle of the crystals will eventually converge to the same limit θ^l for large enough N in both cases (see Supplementary File text S4).

The effectiveness of the proposed assembly rule is validated via both FEA and analytical models. Herein, we assume $a_x = a_y = a_z = a$, and $N_x = N_y = 1/3 \cdot N_z = N$, so that $L_x = L_y = \frac{1}{3}L_z = Na = 75$ mm. A larger dimension in the z-axis can facilitate the measurement of the twist angle in later simulations and experiments. FEA is performed on ABAQUS with geometrical nonlinearity, using nylon PA12 as the constituent material (see Section 2 and text S6). The constants in the analytical model, i.e., θ^l, γ and $\tilde{\gamma}$, are then obtained by minimizing the error between the analytical twist angle and FEA results. We first compare the original and proposed crystal designs under different levels of strains (0.1% and 1.0%) with rod thickness $d = 0.067a$. The results are shown in Fig. 5(a).

While θ/ϵ of the original designs drops significantly as N increases, the twisting angle per uniaxial strain of the proposed designs increases at the beginning, and quickly converges to a stable level, without obvious decrease even up to $N = 20$. The contrasting behavior of the original and proposed crystals are clearly shown in Fig. 5(c). Given that the crystals undergo identical longitudinal strain, the magnitude and spatial distribution of the overall displacement in Fig. 5(c) primarily vary in the centrosymmetric displacement components, namely u_x and u_y . Therefore, a greater magnitude of displacement corresponds to a higher degree of twisting in the structures. The values provided by the analytical model match well with the FEA results, with estimated limits θ/ϵ of 4.64%/ and 4.70%/ under 0.1% and 1.0% strain respectively. This demonstrates excellent scalability of the twist effects with the proposed assembly rules. The proposed crystals with odd and even N exhibit different twist angles for small N but converge to the same value as N increases, which aligns with our previous theoretical analysis. We continued to study the influence of the rod thickness on the scalability, as shown in Fig. 5(b). When assembled with the proposed rules, crystals can still achieve scalable twist effect for various rod thickness $d = 0.027a, 0.067a$ and $0.13a$, converging to estimated limits θ/ϵ of 4.73%/%, 4.70%/%, and 4.48%/%, respectively.

3.2. Scalable twist effects for various metamaterials

Since the analysis and the proposed rules are built on abstract screw theory, they are applicable to various metamaterials with twist effects. Herein, we select two metamaterials in existing research for demonstration, named O-shaped [16] (Fig. 5d) and #-shaped [58] crystals (Fig. 5g), respectively. Although these two metamaterials are different in unit-cell geometry, their basic components (Fig. 5, e and h) contribute constraints screws on HS-1 (Fig. 5, f and i) similar to that in the Z-shaped crystals (Fig. 2, c and d). Therefore, the same 2D description (Fig. 2c) and assembly rules (Fig. 4, a and b) for the Z-shaped crystals can be readily applied to these crystals. The twist angles for all three types of crystals are shown in Fig. 5(j), in which the rods are assumed to have the same square section with a width $d = 0.05a$. It can be noted that, while the twist angles vary for different types of crystals, they all exhibit scalable twist effects with the proposed assembly. Moreover, the angles α between the z-axis and ISA of the constraint screw show an ascending order for O-, #-, and Z-shaped crystals (comparing Fig. 2c, Fig. 5f, and 5i). Based on Eq. (2), the twist angles should follow an inverse order, which is exactly the case for periodic crystals with small N . While this order is lost due to the geometrical frustration in the periodic assembly as N increases, it is preserved in crystals with the proposed assembly. This result further validates the effectiveness of the screw-theory-based analysis and the proposed assembly rule for various metamaterials with

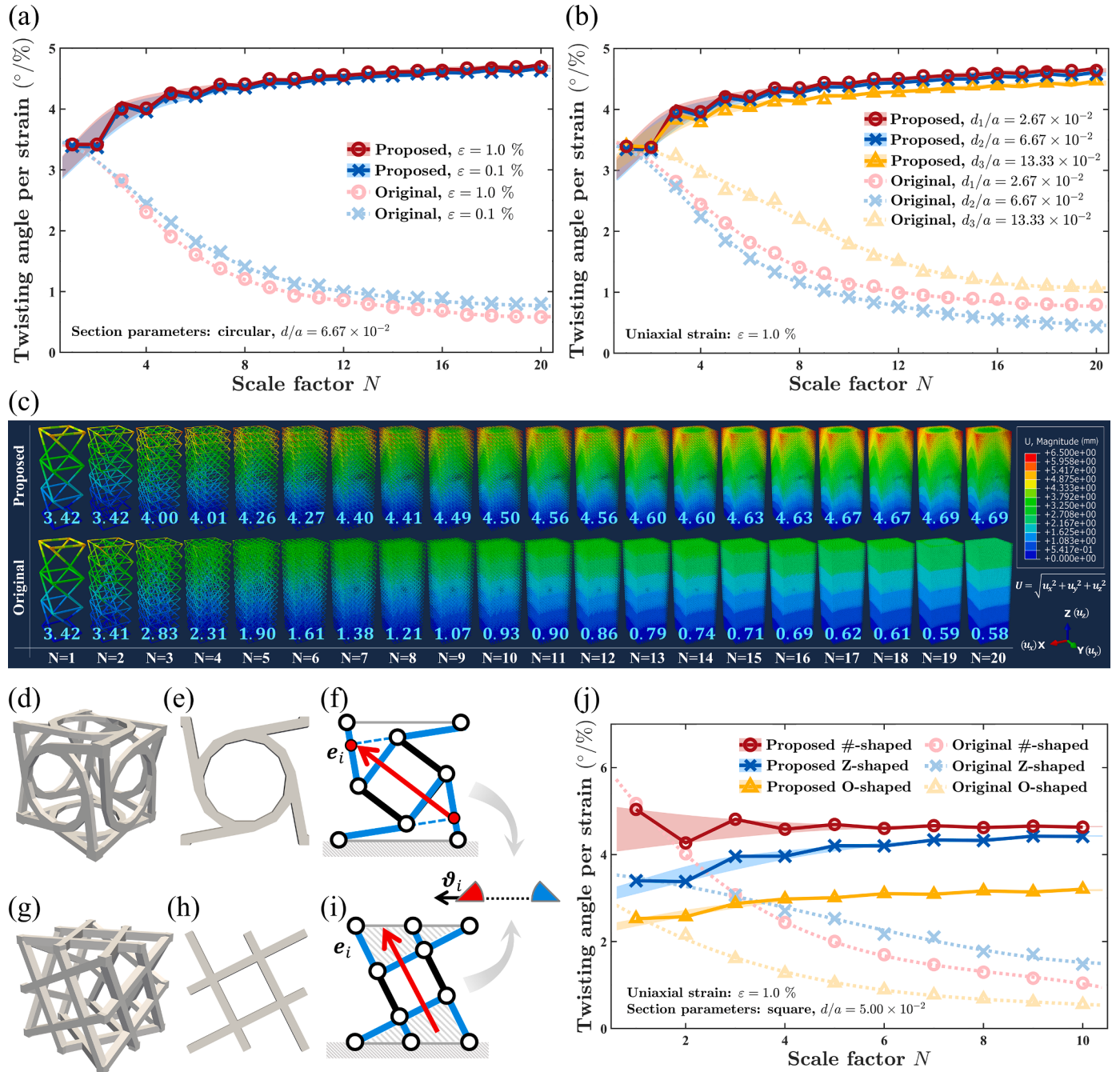


Fig. 5. Analytical and numerical results for different types of crystals. (a) Twisting angles per strain under different strain levels and (b) different diameters of the rods. Scattering dots are obtained from FEA. Solid lines present the analytical results, with the shaded regions showing the variation of angles between odd and even crystals. Dashed lines are fitted splines for the FEA results of the original crystals. (c) Displacement distribution of deformed structures for the proposed and original designs obtained from FEA ($d = 0.067a$, $\varepsilon = 1.0\%$). The value beneath each structure shows its twist angle ($^{\circ}/\%$). (d) O-shaped unit cell, (e) the basic O-shaped component, (f) PRBM of the O-shaped component. The two sets of blue rods rotate around the two red dots, respectively, resulting in an overall constraint screw along the red arrow. (g) #-shaped unit cell, (h) the basic #-shaped component, (i) PRBM of the #-shaped component. The blue sets can be considered rigid parts marked by shaded lines, resulting in an overall constraint screw along the red arrow. (j) Results of different types of crystals.

scalable twist effects.

3.3. Scalable twist effects around multiple axes

The proposed rule can be extended to crystals with twists around multiple axes. A naïve approach is to first assemble the basic components for each axis separately and then directly bond them together. However, unlike previous cases with a single twist axis, coupling and incompatibility can also exist between the twists around different axes,

which is the case with this naïve approach (see Supplementary File text S5 for the detailed proof). To mitigate this issue, we propose to assemble basic components for different twist axes in a staggered pattern, as shown in Fig. 6(a) to (d). Herein, we use the Z-shaped crystals for illustration. The structure shown in Fig. 6(a) is a multi-axis counterpart for the unit-cell design with a single-axis twist in Fig. 2(a), which is named a building block. The original unit-cell designs are placed between cubical frames at the lattice point (Fig. 6, a and e) so that each Z-shaped component only belongs to HS-1 around one specific twist axis

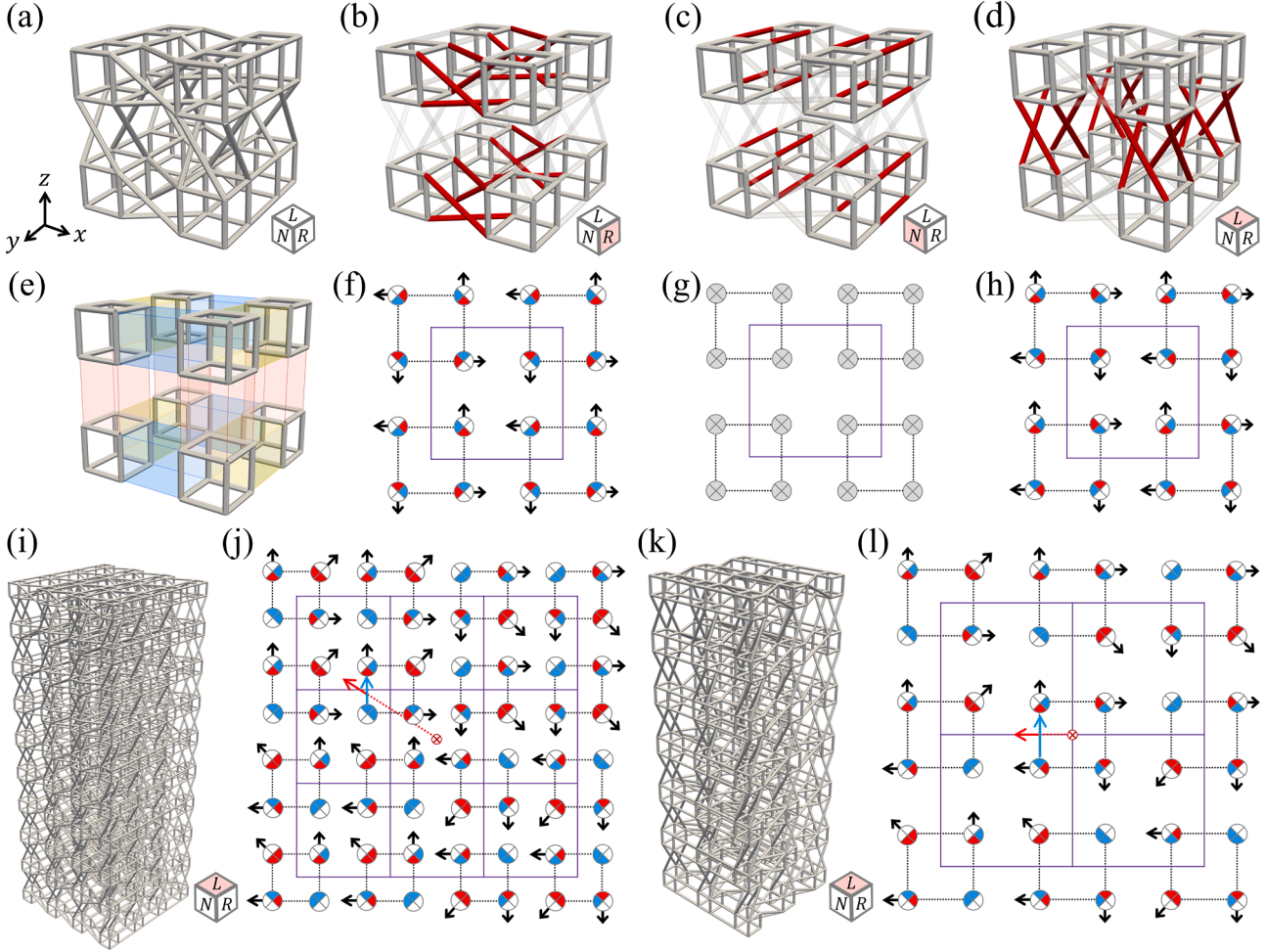


Fig. 6. Assembly rules for crystals with twists around multiple axes. (a) An RNL building block assembled by Z-shaped unit cells (b) with right-handedness in the x-axis, (c) non-handedness in the y-axis and (d) left-handedness in the z-axis. The cubical diagram marks the handedness for different axes on the normal plane, with the plane of interest shaded in red. (e) Cubical frames are placed at the lattice points, connected by different basic components in shaded regions along each axis, along with a 2D description for the component groups in (f) the x-axis, (g) y-axis, and (h) z-axis. The purple box represents lines connecting the lattice points within a building block. (i) RNL crystals with the proposed assembly for even N and (j) its 2D descriptions for components along the z-axis. (k) RNL crystals with the proposed assembly for odd N and (l) its 2D descriptions for components along the z-axis.

(Fig. 6, b to d). The 2D descriptions for component groups on different axes are shown in Fig. 6(f) to (h). In this particular building block, the Z-shaped components are arranged with right-, non-, and left-handedness around the x-, y-, and z-axis, respectively. To assemble a multi-axis counterpart of the original crystal in Fig. 2(m), we can connect cubical frames at all the lattice points with corresponding Z-shaped components following the prototype given in the building block. The newly-created crystal is named the original RNL crystal (R, N, and L refer to the right-, non-, and left-handedness respectively). Note that the scale number N is now measured by the number of building blocks, instead of unit cells, in each dimension. With that, we can directly apply the proposed assembly rules, i.e., $e_{r,i} \cdot \vartheta_i \geq 0$, for component groups along each axis to achieve scalable twist effects, as shown in Fig. 6(i) to (l).

We first studied the twist behaviors of RNL crystals given different rod thicknesses, as shown in Fig. 7(a). We kept the dimensions of the crystal and the simulation settings as that in the single-axis cases. With twists around multiple axes, crystals assembled by the proposed rule can still achieve scalable twist effects for different rod thicknesses, retaining a stable twist angle up to $N = 20$. This scalability is also evident when comparing the deformed structures of the proposed and original RNL crystals in Fig. 7(d). We further validated the simulation by performing physical experiments on 3D-printed samples (Fig. 3a and Fig. 7b, referring to Section 2) with $d = 0.17a$. Due to manufacturing constraints,

we only tested samples up to $N = 8$. As shown in Fig. 7(c), the experimental results matched well with the simulation, with an average relative error of 6.32% for the proposed designs and 13.29% for the original ones. The scalability was also validated under different strain levels in Fig. 7(e). The strain level has a neglectable impact on the twist angle of the proposed crystals, compared with the original assembly. Ulteriorly, we examined the coupling between twists around different axes, by comparing the performance of RNL, NNL, and LLL crystals. As shown in Fig. 7(f) and Fig. S4, the twist angles follow a descending order in the original NNL, RNL, and LLL crystals. It is the coupling between twists in different axes that leads to smaller twist angles in original RNL and LLL crystals. As illustrated in text S5, when different twists are strongly coupled, left-handedness in the z-axis requires right-handedness in the x-axis to be compatible. This can explain why original RNL crystals have larger twist angles than original LLL crystals. However, different combinations of the twists lead to similar scalable twist effects with the proposed assembly. This implies that the coupling between multiple twists is small with the proposed assembly and does not influence the scalability.

4. Conclusions

In this study, we have applied screw theory to provide rigorous

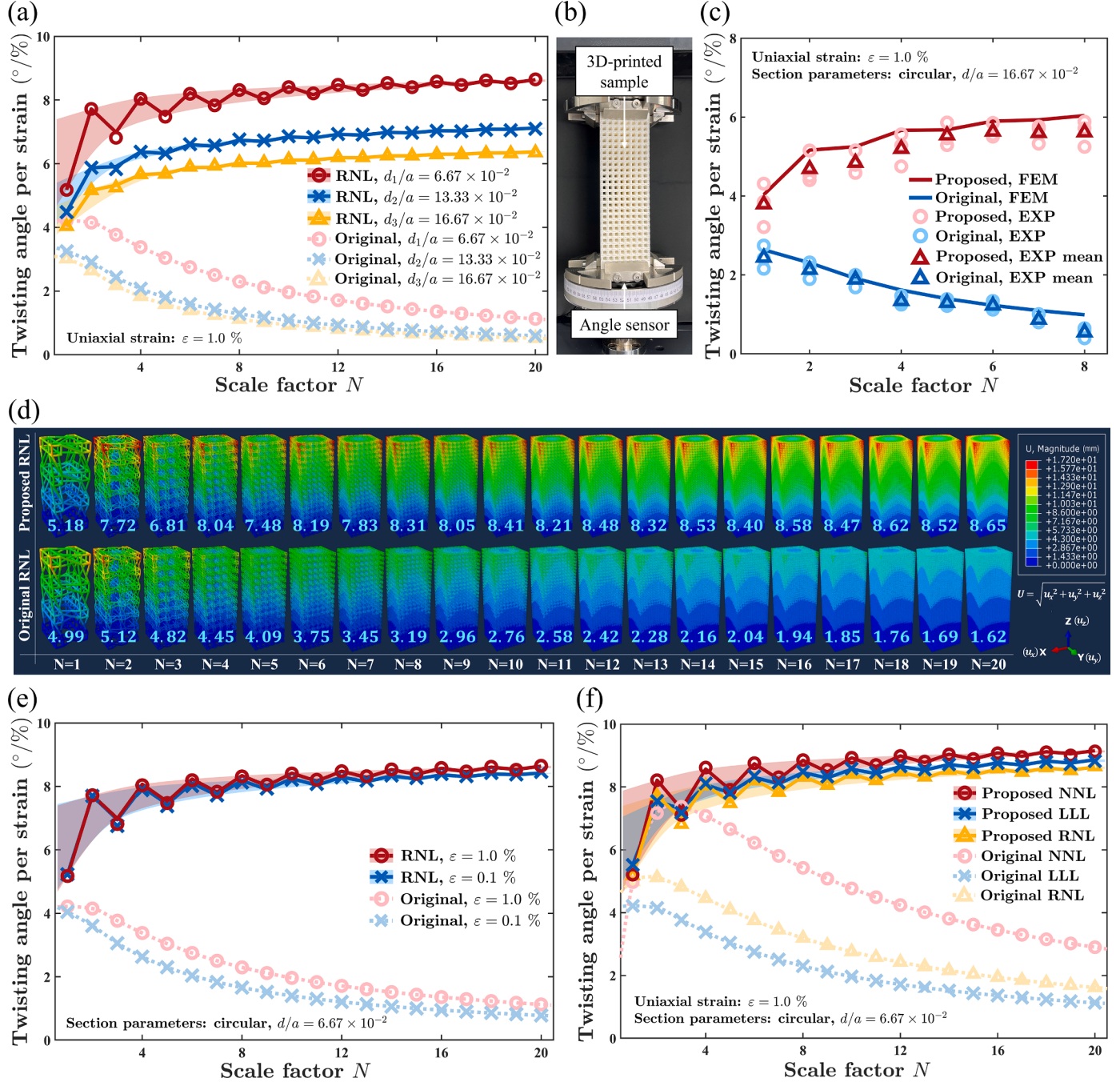


Fig. 7. Results of twist effects around multiple axes. (a) Analytical and numerical results for RNL crystals with different rod thicknesses. (b) Experimental settings. (c) Experimental and simulation results for RNL crystals. Markers with light and dark colors represent the experimental results in multiple replications and their mean values, respectively. The solid lines represent the simulated results. (d) Displacement distribution of deformed structures for the proposed and original RNL crystals obtained from FEA ($d = 0.067a$, $\varepsilon = 1.0\%$). The value beneath each structure shows its twist angle ($^{\circ}/\%$). (e) Analytical and numerical results for RNL crystals under different strain levels, and (f) different combinations of twists.

analysis and comprehensive insights into the twist effect and its loss of scalability. In particular, we find that the loss of scalability is induced by multiple forms of incompatible screw systems among unit cells, which are inherited from the periodic assembly of the crystal. To ensure compatibility, adjacent unit cells should have constrained screws belonging to the same branch of straight lines on HS-1 with the same center axis, and these screws should have the same pitch of motion screws.

Based on this insight, we propose a general rule to assemble a metamaterial crystal with compatible screw systems, enabling scalable twist effects. An analytical model is developed to characterize the relation

between the twist angle and the scale factor. Through numerical simulation, analytical models, and physical experiments, we demonstrated that:

- In all the presented cases, the assembled crystals retain their twist angles and exhibit no obvious decrease even up to a scale factor of 20, demonstrating excellent scalability. Theoretically, the twist angles will converge to their respective constant values that vary for the geometries and loads.
- The proposed rules are general enough to accommodate various forms of unit-cell geometries, different strain levels, geometrical

- parameters, and twists around multiple axes. Following the proposed assembly rules, the design of chirality and microstructures in different axes can be independent. The coupling between multiple-axes twists does not influence the scalability.
- iii) Under the same scale factor, metamaterial crystals assembled by thicker rod components have smaller twists but are still scalable. Also, the twist angles vary for different metamaterial types, which are inherently determined by their respective unit-cell topologies. Nevertheless, by assembling with the proposed rule, they all exhibit scalable twist effects that are unobserved in the original designs.
- The scalable twist effects achieved by the proposed method enable much higher design flexibility for metamaterials to handle complex engineering structures. The weak coupling between twists around multiple axes makes it possible to achieve different twists behaviors along different directions, which is useful for applications that require anisotropic responses, such as transverse wave conversion [28], compliant mechanisms [67,68], micro-robots [26], and actuators and sensors [69,70]. While we only focus on twist effects in this study, the screw-based analysis framework is also a promising tool to guide the design of other metamaterials with various other exotic behaviors.
- ### Author contributions
- L.W. and W.X. contributed equally to the paper; L.W., W.X., Z.L., and P.Z. designed research; L.W. and W.X. performed research; L.W., W.X., Z.L., and P.Z. analyzed data and wrote the paper.
- ### Declaration of Competing Interest
- The authors declare that they have no known competing financial interests or personal relationships that could have appeared to influence the work reported in this paper.
- ### Data availability
- Data will be made available on request.
- ### Acknowledgments
- The authors acknowledge the support from the Natural Science Foundation of Shanghai (Grant No. 21ZR1431500). Liwei Wang acknowledges support from Distinguished Doctoral Scholarships at Shanghai Jiao Tong University.
- ### Supplementary materials
- Supplementary material associated with this article can be found, in the online version, at [doi:10.1016/j.ijmecsci.2023.108579](https://doi.org/10.1016/j.ijmecsci.2023.108579).
- ### References
- [1] Kadic M, Milton GW, Van Hecke M, Wegener M. 3D metamaterials. *Nat Rev Phys* 2019;1:198–210. <https://doi.org/10.1038/s42254-018-0018-y>.
 - [2] Zheludev NI. The road ahead for metamaterials. *Science* 2010;328:582–3. <https://doi.org/10.1126/science.1186756>.
 - [3] Fan J, et al. A review of additive manufacturing of metamaterials and developing trends. *Mater Today* 2021;50:303–28. <https://doi.org/10.1016/j.matto.2021.04.019>.
 - [4] Ha NS, Lu G. A review of recent research on bio-inspired structures and materials for energy absorption applications. *Composites Part B: Engineering* 2020;181:107496. <https://doi.org/10.1016/j.compositesb.2019.107496>.
 - [5] Bertoldi K, Vitelli V, Christensen J, Van Hecke M. Flexible mechanical metamaterials. *Nat Rev Mater* 2017;2:17066. <https://doi.org/10.1038/natrevmats.2017.66>.
 - [6] Yu X, Zhou J, Liang H, Jiang Z, Wu L. Mechanical metamaterials associated with stiffness, rigidity and compressibility: a brief review. *Prog Mater Sci* 2018;94:114–73. <https://doi.org/10.1016/j.pmatsci.2017.12.003>.
 - [7] Pan F, et al. 3D pixel mechanical metamaterials. *Adv Mater* 2019;31:1900548. <https://doi.org/10.1002/adma.201900548>.
 - [8] Jiang Y, et al. Auxetic mechanical metamaterials to enhance sensitivity of stretchable strain sensors. *Adv Mater* 2018;30:1706589. <https://doi.org/10.1002/adma.201706589>.
 - [9] Fu M, Liu F, Hu L. A novel category of 3D chiral material with negative Poisson's ratio. *Compos Sci Technol* 2018;160:111–8. <https://doi.org/10.1016/j.compsitech.2018.03.017>.
 - [10] Wang J, Luo X, Wang K, Yao S, Peng Y. On impact behaviors of 3D concave structures with negative Poisson's ratio. *Compos Struct* 2022;298. <https://doi.org/10.1016/j.compstruct.2022.115999>.
 - [11] Berwind MF, Kamas A, Eberl C. A hierarchical programmable mechanical metamaterial unit cell showing metastable shape memory. *Adv Eng Mater* 2018;20:1800771. <https://doi.org/10.1002/adem.201800771>.
 - [12] Liu K, Tachi T, Paulino GH. Invariant and smooth limit of discrete geometry folded from bistable origami leading to multistable metasurfaces. *Nat Commun* 2019;10:4238. <https://doi.org/10.1038/s41467-019-11935-x>.
 - [13] Kadic M, Bückmann T, Stenger N, Thiel M, Wegener M. On the practicability of pentamode mechanical metamaterials. *Appl Phys Lett* 2012;100:191901. <https://doi.org/10.1063/1.4709436>.
 - [14] Zhao A, et al. Design and experimental verification of a broadband multiphase pentamode material. *Phys Rev Appl* 2022;18:034001. <https://doi.org/10.1103/PhysRevApplied.18.034001>.
 - [15] Fernandez-Corbaton I, et al. New twists of 3D chiral metamaterials. *Adv Mater* 2019;31:1807742. <https://doi.org/10.1002/adma.201807742>.
 - [16] Frenzel T, Kadic M, Wegener M. Three-dimensional mechanical metamaterials with a twist. *Science* 2017;358:1072–4. <https://doi.org/10.1126/science.aoa4640>.
 - [17] Prall D, Lakes RS. Properties of a chiral honeycomb with a poisson's ratio of -1. *Int J Mech Sci* 1997;39:305–14. [https://doi.org/10.1016/s0020-7403\(96\)00025-2](https://doi.org/10.1016/s0020-7403(96)00025-2).
 - [18] Eringen AC. Microcontinuum field theories: I. foundations and solids. Springer Science & Business Media; 2012.
 - [19] Liu D, et al. Spider dragline silk as torsional actuator driven by humidity. *Sci Adv* 2019;5:eau9183. <https://doi.org/10.1126/sciadv.aau9183>.
 - [20] Cohen N, Eisenbach CD. Humidity-driven supercontraction and twist in spider silk. *Phys Rev Lett* 2022;128:098101. <https://doi.org/10.1103/PhysRevLett.128.098101>.
 - [21] Gross P, et al. Quantifying how DNA stretches, melts and changes twist under tension. *Nat Phys* 2011;7:731–6. <https://doi.org/10.1038/nphys2002>.
 - [22] Emuna N, Cohen N. Inversion and perversian in twist incompatible isotropic tubes. *Extreme Mech Lett* 2021;46:101303. <https://doi.org/10.1016/j.eml.2021.101303>.
 - [23] Xu X, et al. Physical realization of elastic cloaking with a polar material. *Phys Rev Lett* 2020;124. <https://doi.org/10.1103/physrevlett.124.114301>.
 - [24] Wang L, et al. Mechanical cloak via data-driven aperiodic metamaterial design. *Proc Natl Acad Sci* 2022;119. <https://doi.org/10.1073/pnas.2122185119>.
 - [25] Lee H, et al. 3D-printed programmable tensegrity for soft robotics. *Science Robotics* 2020;5:eaey9024. <https://doi.org/10.1126/scirobotics.ayy9024>.
 - [26] Cui H, et al. Design and printing of proprioceptive three-dimensional architected robotic metamaterials. *Science* 2022;376:1287–93. <https://doi.org/10.1126/science.abn0090>.
 - [27] Frenzel T, Kopfler J, Jung E, Kadic M, Wegener M. Ultrasound experiments on acoustical activity in chiral mechanical metamaterials. *Nat Commun* 2019;10:3384. <https://doi.org/10.1038/s41467-019-11366-8>.
 - [28] Chen Y, Frenzel T, Guenneau S, Kadic M, Wegener M. Mapping acoustical activity in 3D chiral mechanical metamaterials onto micropolar continuum elasticity. *J Mech Phys Solids* 2020;137. <https://doi.org/10.1016/j.jmps.2020.103877>.
 - [29] Goswami D, et al. Mechanical metamaterials with programmable compression-twist coupling. *Smart Mater Struct* 2021;30:015005. <https://doi.org/10.1088/1361-665x/abc182>.
 - [30] Tabacu S, Negrea RF, Negrea D. Experimental, numerical and analytical investigation of 2D tetra-anti-chiral structure under compressive loads. *Thin Walled Struct* 2020;155. <https://doi.org/10.1016/j.tws.2020.106929>.
 - [31] Hamzehei R, Rezaei S, Kadkhodapour J, Anaraki AP, Mahmoudi A. 2D triangular anti-trichiral structures and auxetic stents with symmetric shrinkage behavior and high energy absorption. *Mech Mater* 2020;142:103291. <https://doi.org/10.1016/j.mechmat.2019.103291>.
 - [32] Zhu Y, Zeng Z, Wang Z-P, Poh LH, Shao Y. Hierarchical hexachiral auxetics for large elasto-plastic deformation. *Mater Res Express* 2019;6:085701. <https://doi.org/10.1088/2053-1591/ab1a22>.
 - [33] Surjadi JU, et al. Mechanical metamaterials and their engineering applications. *Adv Eng Mater* 2019;21:1800864. <https://doi.org/10.1002/adem.201800864>.
 - [34] Han SC, Kang DS, Kang K. Two nature-mimicking auxetic materials with potential for high energy absorption. *Mater Today* 2019;26:30–9. <https://doi.org/10.1016/j.matto.2018.11.004>.
 - [35] Zong H, Zhang H, Wang Y, Wang MY, Fuh JYH. On two-step design of microstructure with desired Poisson's ratio for AM. *Mater Des* 2018;159:90–102. <https://doi.org/10.1016/j.matdes.2018.08.032>.
 - [36] Fu M-H, Zheng B-B, Li W-H. A novel chiral three-dimensional material with negative Poisson's ratio and the equivalent elastic parameters. *Compos Struct* 2017;176:442–8. <https://doi.org/10.1016/j.compstruct.2017.05.027>.
 - [37] Li J, Ha CS, Lakes RS. Observation of squeeze-twist coupling in a chiral 3D isotropic lattice. *Phys Status Solidi* 2019;257. <https://doi.org/10.1002/psb.201900140>.

- [38] Xu W, Liu Z, Wang L, Zhu P. 3D chiral metamaterial modular design with highly-tunable tension-twisting properties. *Materials Today Communications* 2022;30. <https://doi.org/10.1016/j.mtcomm.2021.103006>.
- [39] Ha CS, Plesha ME, Lakes RS. Chiral three-dimensional lattices with tunable Poisson's ratio. *Smart Mater Struct* 2016;25. <https://doi.org/10.1088/0964-1726/25/5/054005>.
- [40] Chen Y, Frenzel T, Zhang Q, Kadic M, Wegener M. Cubic metamaterial crystal supporting broadband isotropic chiral phonons. *Phys Rev Mater* 2021;5:025201. <https://doi.org/10.1103/PhysRevMaterials.5.025201>.
- [41] Meng L, et al. An emerging class of hyperbolic lattice exhibiting tunable elastic properties and impact absorption through chiral twisting. *Extreme Mech Lett* 2020; 40. <https://doi.org/10.1016/j.eml.2020.100869>.
- [42] Duan S, Xi L, Wen W, Fang D. A novel design method for 3D positive and negative Poisson's ratio material based on tension-twist coupling effects. *Compos Struct* 2020;236. <https://doi.org/10.1016/j.compstruct.2020.111899>.
- [43] Zheng B-B, Zhong R-C, Chen X, Fu M-H, Hu L-L. A novel metamaterial with tension-torsion coupling effect. *Mater Des* 2019;171. <https://doi.org/10.1016/j.matdes.2019.107700>.
- [44] Wu W, et al. Mechanical design and multifunctional applications of chiral mechanical metamaterials: a review. *Mater Des* 2019;180. <https://doi.org/10.1016/j.matdes.2019.107950>.
- [45] Ebrahimi H, Mousanezhad D, Nayeb-Hashemi H, Norato J, Vaziri A. 3D cellular metamaterials with planar anti-chiral topology. *Mater Des* 2018;145:226–31. <https://doi.org/10.1016/j.matdes.2018.02.052>.
- [46] Lipton JL, et al. Handedness in shearing auxetics creates rigid and compliant structures. *Science* 2018;360:632–5. <https://doi.org/10.1126/science.aar4586>.
- [47] Ma C, et al. Experimental and simulation investigation of the reversible bi-directional twisting response of tetra-chiral cylindrical shells. *Compos Struct* 2018; 203:142–52. <https://doi.org/10.1016/j.compstruct.2018.07.013>.
- [48] Lu Q, Qi D, Li Y, Xiao D, Wu W. Impact energy absorption performances of ordinary and hierarchical chiral structures. *Thin Walled Struct* 2019;140:495–505. <https://doi.org/10.1016/j.tws.2019.04.008>.
- [49] Wu W, et al. Compression twist deformation of novel tetrachiral architected cylindrical tube inspired by towel gourd tendrils. *Extreme Mech Lett* 2018;20: 104–11. <https://doi.org/10.1016/j.eml.2018.02.001>.
- [50] Farrell DT, McGinn C, Bennett GJ. Extension twist deformation response of an auxetic cylindrical structure inspired by deformed cell ligaments. *Compos Struct* 2020;238. <https://doi.org/10.1016/j.compstruct.2020.111901>.
- [51] Huang H-H, Wong B-L, Chou Y-C. Design and properties of 3D-printed chiral auxetic metamaterials by reconfigurable connections. *Phys Status Solidi* 2016;253: 1557–64. <https://doi.org/10.1002/pssb.201600027>.
- [52] Xia R, et al. Mechanical properties of 3D isotropic anti-tetrachiral metastructure. *Phys Status Solidi* 2018;255:1700343. <https://doi.org/10.1002/pssb.201700343>.
- [53] Wu W, et al. Deformation mechanism of innovative 3D chiral metamaterials. *Sci Rep* 2018;8. <https://doi.org/10.1038/s41598-018-30737-7>.
- [54] Fleisch M, et al. Chiral-based mechanical metamaterial with tunable normal-strain shear coupling effect. *Eng Struct* 2023;284:115952. <https://doi.org/10.1016/j.engstruct.2023.115952>.
- [55] Ziemke P, Frenzel T, Wegener M, Gumbsch P. Tailoring the characteristic length scale of 3D chiral mechanical metamaterials. *Extreme Mech Lett* 2019;32:100553. <https://doi.org/10.1016/j.eml.2019.100553>.
- [56] Zhao W, Zhu J, Liu L, Leng J, Liu Y. A bio-inspired 3D metamaterials with chirality and anti-chirality topology fabricated by 4D printing. *International Journal of Smart and Nano Materials* 2023;14:1–20. <https://doi.org/10.1080/19475411.2022.2120110>.
- [57] Chen W, Huang X. Topological design of 3D chiral metamaterials based on couple-stress homogenization. *J Mech Phys Solids* 2019;131:372–86. <https://doi.org/10.1016/j.jmps.2019.07.014>.
- [58] Li X, Yang Z, Lu Z. Design 3D metamaterials with compression-induced-twisting characteristics using shear-compression coupling effects. *Extreme Mech Lett* 2019; 29. <https://doi.org/10.1016/j.eml.2019.100471>.
- [59] Farrugia PS, Gatt R, Grima JN. A novel three-dimensional anti-tetrachiral honeycomb. *Phys Status Solidi* 2018;256:1800473. <https://doi.org/10.1002/pssb.201800473>.
- [60] Jenett B, et al. Discretely assembled mechanical metamaterials. *Sci Adv* 2020;6: eabc9943. <https://doi.org/10.1126/sciadv.abc9943>.
- [61] Ha CS, Plesha ME, Lakes RS. Chiral three-dimensional isotropic lattices with negative Poisson's ratio. *Phys Status Solidi* 2016;253:1243–51. <https://doi.org/10.1002/pssb.201600055>.
- [62] Zhang W, Bai X, Hou B, Sun Y, Han X. Mechanical properties of the three-dimensional compression-twist cellular structure. *J Reinf Plast Compos* 2019;39: 260–77. <https://doi.org/10.1177/0731684419888588>.
- [63] Chen X, He T, Hu Y, Feng M. A 3D dislocated re-entrant structure with compression-twist coupling effect. *Smart Mater Struct* 2023;32:055009. <https://doi.org/10.1088/1361-665x/acc621>.
- [64] Duan S, Wen W, Fang D. A predictive micropolar continuum model for a novel three-dimensional chiral lattice with size effect and tension-twist coupling behavior. *J Mech Phys Solids* 2018;121:23–46. <https://doi.org/10.1016/j.jmps.2018.07.016>.
- [65] Frenzel T, et al. Large characteristic lengths in 3D chiral elastic metamaterials. *Commun Mater* 2021;2. <https://doi.org/10.1038/s43246-020-00107-w>.
- [66] Sun T, Yang S, Lian B. Finite and instantaneous screw theory in robotic mechanism. Springer Nature; 2020.
- [67] Shaw LA, et al. Computationally efficient design of directionally compliant metamaterials. *Nat Commun* 2019;10. <https://doi.org/10.1038/s41467-018-08049-1>.
- [68] Morrison T, Su H-J. Stiffness modeling of a variable stiffness compliant link. In: 153; 2020, 104021. <https://doi.org/10.1016/j.mechmachtheory.2020.104021>.
- [69] Truby RL, Chin L, Zhang A, Rus D. Fluidic innervation sensorizes structures from a single build material. *Sci Adv* 2022;8:eabq4385. <https://doi.org/10.1126/sciadv.abq4385>.
- [70] Kaarthik P, Sanchez FL, Avtges J, Truby RL. Motorized, untethered soft robots via 3D printed auxetics. *Soft Matter* 2022;18:8229–37. <https://doi.org/10.1039/d2sm00779g>.